A Comparison of Frequency Downshift Models of Wave Trains on Deep Water

John D. Carter
Diane Henderson
Isabelle Butterfield

September 25, 2018

Abstract

Frequency downshift (FD) in wave trains on deep water occurs when a measure of the frequency, typically the spectral peak or the spectral mean, decreases as the waves travel down a tank or across the ocean. Many FD models rely on wind or wave breaking. We consider seven models that do not include these effects and compare their predictions with four sets of experiments that also do not include these effects. The models are the (i) nonlinear Schrödinger equation (NLS), (ii) dissipative NLS equation (dNLS), (iii) Dysthe equation, (iv) viscous Dysthe equation (vDysthe), (v) Gordon equation (Gordon) (which has a free parameter), (vi) Islas-Schober equation (IS) (which has a free parameter), and (vii) a new model, the dissipative Gramstad-Trulsen (dGT) equation. The dGT equation has no free parameters and addresses some of the difficulties associated with the Dysthe and vDysthe equations. We compare a measure of overall error and the evolution of the spectral amplitudes, mean, and peak. We find: (i) The NLS and Dysthe equations do not accurately predict the measured spectral amplitudes. (ii) The Gordon equation, which is a successful model of FD in optics, does not accurately model FD in water waves, regardless of the choice of free parameter. (iii) The dNLS, vDysthe, dGT, and IS (with optimized free parameter) models all do a reasonable job predicting the measured spectral amplitudes, but none captures all spectral evolutions. (iv) The vDysthe, dGT, and IS (with optimized free parameter) models do the best at predicting the observed evolution of the spectral peak and the spectral mean. (v) The IS model, optimized over its free parameter, has the smallest overall error for three of the four experiments. The vDysthe equation has the smallest overall error in the other experiment.

1 Introduction

In a series of classic experiments, Lake *et al.* [16] and Lake & Yuen [15] examined the evolution of wave trains on deep water. A paddle at one end of a narrow tank created a nearly two-dimensional, nearly monochromatic wave train with a particular frequency. As the wave train traveled down the tank, it became modulated due to the growth of the Benjamin-Feir instability. Further down the tank, the wave train returned to a nearly monochromatic form, however the dominant frequency was lower than the frequency created by the paddle. This shift to a lower frequency in wave trains is referred to as frequency downshifting (FD). Subsequent experiments, including those in Su *et al.* [24] and Melville [20], demonstrated that the amplitude of the lower sideband grew and eventually overtook that of the carrier wave. In 2005, Segur *et al.* [22], conducted similar experiments and found that FD provided a means of distinguishing waves with "small or moderate" amplitudes, in which FD was not observed, and waves with "large" amplitudes, in which FD was observed. In particular, they used successfully a nonlinear Schrödinger equation with linear damping to describe waves with small or moderate amplitudes. Since that equation does not allow for FD, they considered waves that exhibited FD to have large amplitudes.

Many mathematical justifications for FD have been proposed. Most, including Trulsen & Dysthe [26], Hara & Mei [9], Kato & Oikawa [13], Islas-Schober [11], Brunetti & Kasparian [2], and Brunetti *et al.* [3], rely on wind and/or wave breaking as mechanisms for FD. As there was no wind nor wave breaking in the Segur *et al.* [22] experiments, there must be another mechanism for FD. A clear understanding of frequency downshifting and the mechanisms behind it will lead to a better understanding of the evolution of swell

and how wave energy is transported across the ocean. In this paper, we explore possible mathematical models/mechanisms for FD in the absence of wind and/or wave breaking using numerics and experiments.

Three quantities that are commonly used to quantify FD are the linear momentum,

$$\mathcal{P}(\chi) = \frac{i}{2L}\int_0^L \left(BB_\xi^* - B_\xi B^*\right)d\xi, \tag{1}$$

the spectral peak, ω_p, and the spectral mean, ω_m. The spectral peak is the frequency corresponding to the Fourier mode with largest magnitude. The spectral mean is defined by the ratio

$$\omega_m = \frac{\mathcal{P}}{\mathcal{M}}, \tag{2}$$

where

$$\mathcal{M}(\chi) = \frac{1}{L}\int_0^L |B|^2 d\xi. \tag{3}$$

Here B is a dimensionless measure of the complex envelope of a slowly evolving, nearly monochromatic train of plane waves, χ is dimensionless distance down the tank, ξ is dimensionless time, and L is the dimensionless ξ-period of B. (In this paper, all dimensional variables have overbars. For example, $\bar{x}$ is the dimensional horizontal coordinate.) There is not a generally agreed upon definition for FD in the literature. Some authors have defined FD to be a decrease in ω_m, some have defined FD to be a decrease in ω_p, and others have defined it to be a decrease in $\mathcal{P}$. In hopes of reducing confusion, we use two definitions of FD. We state that FD in the spectral mean sense occurs if ω_m decreases and that FD in the spectral peak sense occurs if ω_p decreases. For example, Lake & Yuen [15] observed a decrease in ω_p. Segur *et al.* [22] observed that ω_p and ω_m decreased together.

The focus of this paper is to compare measurements of waves from one experiment that did not exhibit downshift and three that exhibited downshift with predictions from seven mathematical models that are in the literature. The models include: the classical cubic nonlinear Schrödinger equation [30, 25] (NLS), the Dysthe equation [6] (Dysthe), the dissipative NLS equation [22, 5] (dNLS), the viscous Dysthe equation [4] (vDysthe), the Islas-Schober equation [11] (IS), the Gordon equation [7] (Gordon), and a new model presented herein, which we call the dissipative Gramstad-Trulsen equation (dGT), a dissipative generalization of the model derived by Gramstad-Trulsen [8]. We focus on FD and frequency upshift (FU) in both the spectral mean and spectral peak senses. We show that the conservative models, NLS and Dysthe, do not accurately predict the measured spectral amplitudes. We show that the Gordon model cannot accurately model FD in water wave experiments because it does not accurately model the evolution of $\mathcal{P}$ regardless of the choice of the free parameter. We show that dNLS, vDysthe, IS, and dGT do the best at predicting the evolution of the spectral peak and mean. The Islas-Schober model also has a free parameter. We show that with the optimal (defined below) parameter choice, it typically provides the most accurate model of FD.

The remainder of this paper is organized as follows. Section 2 introduces the model equations and their properties. Section 3 contains a description of the experimental facility and procedures. Section 4 contains results of the comparisons between experiments and predictions. Finally, Section 5 contains a summary and a list of some possible future work.

2 Model equations

Wu *et al.* [28] proposed the following system for an infinitely-deep, weakly dissipative, two-dimensional fluid

$$\bar{\phi}_{\bar{x}\bar{x}} + \bar{\phi}_{\bar{z}\bar{z}} = 0, \qquad \text{for } -\infty < \bar{z} < \bar{\eta}, \tag{4a}$$

$$\bar{\phi}_{\bar{t}} + \frac{1}{2}\left(\bar{\phi}_{\bar{x}}^2 + \bar{\phi}_{\bar{z}}^2\right) + \bar{g}\bar{\eta} = -\bar{\alpha}\bar{\phi}_{\bar{z}\bar{z}}, \qquad \text{at } \bar{z} = \bar{\eta}, \tag{4b}$$

$$\bar{\phi}_{\bar{z}} = \bar{\eta}_{\bar{t}} + \bar{\eta}_{\bar{x}}\bar{\phi}_{\bar{x}}, \qquad \text{at } \bar{z} = \bar{\eta}, \tag{4c}$$

$$|\nabla\bar{\phi}| \to 0, \qquad \text{as } \bar{z} \to -\infty. \tag{4d}$$

Here $\bar{\phi} = \bar{\phi}(\bar{x}, \bar{z}, \bar{t})$ represents the velocity potential of the fluid, $\bar{\eta} = \bar{\eta}(\bar{x}, \bar{t})$ represents the free-surface displacement, $\bar{x}$ is the horizontal coordinate, $\bar{z}$ is the vertical coordinate, $\bar{t}$ is the temporal coordinate, $\bar{g}$ represents the acceleration due to gravity, and $\bar{\alpha} > 0$ is a constant such that $\bar{\alpha}\bar{\phi}_{\bar{z}\bar{z}}$ represents dissipation from all sources. The classical Euler equations are obtained from this system by setting $\bar{\alpha} = 0$. We note that Dias *et al.* [5] derived a version of (4) that includes an additional (viscous/dissipative) term in equation (4c) starting from a weakly viscous (linear) system. However, that system does not conserve mass.

Wu *et al.* [28] numerically integrated (4) and compared with the Segur *et al.* [22] experimental results. Wu *et al.* [28] used the experimentally measured damping rate for $\bar{\alpha}$ that was obtained from the exponential decay of $\mathcal{M}$. Their corresponding predictions from (4) for the evolution of $\mathcal{P}$ and for the Fourier amplitudes of three frequency components of the spectrum agreed well with measurements.

Four of the models for FD considered herein may be derived from (4). NLS and Dysthe can be derived when $\bar{\alpha} = 0$ and dNLS and vDysthe can be derived when $\bar{\alpha} > 0$. These derivations are outlined below. Two of the models, IS and Gordon, also follow the derivation (with $\bar{\alpha} = 0$) but have additional, ad-hoc terms added, with free parameters. The last model, dGT, is obtained from the Gramstad-Trulsen equation (GT) [8] by adding three ad-hoc terms (but no free parameters) that allow for dissipation. The GT equation can be derived from 4 with $\bar{\alpha} = 0$. All of these models are discussed in more detail below.

2.1 Asymptotic models

In order to model the evolution of a slowly modulated wave train, assume

$$\bar{\eta}(\bar{x}, \bar{t}, \bar{X}, \bar{T}) = \epsilon^3 \bar{H}(\bar{X}, \bar{T}) + \epsilon \bar{B}(\bar{X}, \bar{T}) \mathrm{e}^{i\bar{\omega}_0 \bar{t} - i\bar{k}_0 \bar{x}} + \epsilon^2 \bar{B}_2(\bar{X}, \bar{T}) \mathrm{e}^{2(i\bar{\omega}_0 \bar{t} - i\bar{k}_0 \bar{x})} + \cdots + c.c., \tag{5a}$$

$$\begin{aligned} \bar{\phi}(\bar{x}, \bar{z}, \bar{t}, \bar{X}, \bar{Z}, \bar{T}) = \epsilon^2 \bar{\Phi}(\bar{X}, \bar{Z}, \bar{T}) + \epsilon \bar{A}_1(\bar{X}, \bar{Z}, \bar{T}) \mathrm{e}^{\bar{k}_0 \bar{z} + i\bar{\omega}_0 \bar{t} - i\bar{k}_0 \bar{x}} \\ + \epsilon^2 \bar{A}_2(\bar{X}, \bar{Z}, \bar{T}) \mathrm{e}^{2(\bar{k}_0 \bar{z} + i\bar{\omega}_0 \bar{t} - i\bar{k}_0 \bar{x})} + \cdots + c.c., \end{aligned} \tag{5b}$$

where $\bar{\omega}_0 \in \mathbb{R}$ and $\bar{k}_0 > 0$ are constants representing the frequency and wavenumber of the carrier wave respectively, $\epsilon = 2\bar{a}_0 \bar{k}_0 \ll 1$ is the dimensionless wave steepness, $\bar{a}_0$ represents a typical wave amplitude, and *c.c.* stands for complex conjugate. The slow, dimensional variables are defined by $\bar{X} = \epsilon \bar{x}$, $\bar{Z} = \epsilon \bar{z}$, and $\bar{T} = \epsilon \bar{t}$. We assume that dissipative effects are small by setting $\bar{\alpha} = \epsilon^2 \tilde{\alpha}$. Note that the sign in the exponentials in equation (5) is different than the choice typically used in the literature. This choice is made so that a decrease in the experimental frequency corresponds to a decrease in the frequency in equations (4)-(5) and in the asymptotic models introduced below. Finally, in order to compare with our unidirectional experiments, we only consider waves that travel to the right and therefore require $\bar{\omega}_0 > 0$.

Substituting equation (5) into (4) gives the deep-water linear dispersion relationship

$$\bar{\omega}_0^2 = \bar{g}\bar{k}_0, \tag{6}$$

at leading order. Next, nondimensionalize and transform to enter a coordinate frame moving with the linear group velocity, $\frac{\bar{\omega}_0}{2\bar{k}_0}$, by introducing the change of variables

$$\xi = \bar{\omega}_0 \bar{T} - 2\bar{k}_0 \bar{X}, \tag{7a}$$

$$\chi = \epsilon \bar{k}_0 \bar{X}, \tag{7b}$$

$$\bar{k}_0 \bar{B}(\bar{X}, \bar{T}) = B(\xi, \chi), \tag{7c}$$

$$\frac{\bar{k}_0^2}{\bar{\omega}_0} \tilde{\alpha} = \delta, \tag{7d}$$

where ξ is nondimensional time, χ is nondimensional distance down the tank, B is the dimensionless complex amplitude of the envelope, and δ is the nondimensional dissipation parameter. The vDysthe equation,

$$iB_\chi + B_{\xi\xi} + 4|B|^2 B + i\delta B + \epsilon\Big(- 8iB^2 B_\xi^* - 32i|B|^2 B_\xi - 8\Big(\mathcal{H}\big(|B|^2\big)\Big)_\xi B + 5\delta B_\xi \Big) = 0, \tag{8}$$

arises as a solvability condition at $\mathcal{O}(\epsilon^4)$. Here $\mathcal{H}$ is the Hilbert transform defined by

$$\mathcal{H}\big(f(\xi)\big) = \sum_{k=-\infty}^{\infty} -i\,\mathrm{sgn}(k)\hat{f}(k)\mathrm{e}^{2\pi ik\xi/L}, \tag{9}$$

and the Fourier transform of a function $f(x)$ is defined by

$$\hat{f}(k) = \frac{1}{L}\int_0^L f(\xi)\mathrm{e}^{-2\pi ik\xi/L}d\xi, \tag{10}$$

where L is the ξ-period of the experimental time series. Carter & Govan [4] showed that the vDysthe equation accurately models data from experiments in which frequency downshift was observed and experiments in which frequency downshift was not observed. Kimmoun *et al.* [14] showed that the vDysthe equation accurately models data from experiments conducted in a much larger experimental tank.

When $\delta = \epsilon = 0$, the viscous Dysthe equation reduces to the NLS equation,

$$iB_\chi + B_{\xi\xi} + 4|B|^2B = 0. \tag{11}$$

The NLS equation was first derived as a model of water waves by Zakharov [30]. It has been well studied; see for example Ablowitz & Segur [1] and Sulem & Sulem [25].

When $\epsilon = 0$, the vDysthe equation reduces to the dNLS equation,

$$iB_\chi + B_{\xi\xi} + 4|B|^2B + i\delta B = 0. \tag{12}$$

This equation has been been shown to compare well with experiments in which FD did not occur; see for example Segur *et al.* [22] and Wu *et al.* [28].

When $\delta = 0$, the vDysthe equation reduces to the Dysthe [6] equation, which is also known as the modified NLS equation,

$$iB_\chi + B_{\xi\xi} + 4|B|^2B + \epsilon\Big(-8iB^2B_\xi^* - 32i|B|^2B_\xi - 8\Big(\mathcal{H}\big(|B|^2\big)\Big)_\xi B\Big) = 0. \tag{13}$$

Lo & Mei [18] compared numerical simulations with experimental measurements and showed that the Dysthe equation more accurately predicts the evolution of wave trains than does the NLS equation.

In 2011, Gramstad-Trulsen [8] derived a Hamiltonian fourth-order NLS-type equation (in other words, a Hamiltonian version of the Dysthe equation). Islas-Schober [11] proposed the following dissipative generalization of this equation

$$iB_\chi + B_{\xi\xi} + 4|B|^2B + i\delta B + \epsilon\Big(-32i|B|^2B_\xi + (-8+i\beta_1)\Big(\mathcal{H}\big(|B|^2\big)\Big)_\xi B\Big) = 0, \tag{14}$$

where β_1 is an arbitrary constant. We refer to this equation as the IS equation. The constant β_1 must be positive in order for that term to represent additional dissipative effects (see equation (19a)).

We propose a different generalization of the Gramstad-Trulsen equation

$$iB_\chi + B_{\xi\xi} + 4|B|^2B + i\delta B + \epsilon\Big(-32i|B|^2B_\xi - 8\Big(\mathcal{H}\big(|B|^2\big)\Big)_\xi B + 5\delta B_\xi\Big) - 10i\epsilon^2\delta B_{\xi\xi} = 0, \tag{15}$$

as a model for the evolution of wave trains on deep water. The three terms including δ come from extending the derivation of the vDysthe equation one order higher. We refer to this equation as the dissipative Gramstad-Trulsen (dGT) equation. This equation avoids some of the difficulties exhibited by the Dysthe and vDysthe equations as well as the free parameter of IS. These difficulties are discussed along with the properties of these equations in the next section.

Frequency downshift has also been observed in experiments on electromagnetic waves in optical fibers [21]. Gordon [7] derived the following equation for the complex amplitude of the slowly varying envelope of the carrier wave by including Raman effects

$$iB_\chi + B_{\xi\xi} + 4|B|^2B + \epsilon\beta_2\big(|B|^2\big)_\xi B = 0, \tag{16}$$

where $\beta_2 > 0$ is an arbitrary constant in the water waves setting. We refer to this equation as the Gordon equation. Although electromagnetic waves in optical fibers and surface water waves are quite different physically, both can be accurately modeled using NLS-type equations. It is reasonable to compare (16) with data to determine whether or not a β_2 exists for water waves. Therefore, we include this optics model of FD in our study of FD in water waves. (Though, in Section 4, we show that no such constant exists for our water wave experiments.)

2.2 Model properties

The conservative (non-dissipative) asymptotic models for the evolution of wave trains on deep water, NLS, Dysthe, and GT are derived from Euler's equations, (4) with $\bar{\alpha} = 0$. Euler's equations preserve $\mathcal{M}$, $\mathcal{P}$, and ω_m. FD is a phenomenon that breaks this structure of the system. In particular, FD requires for at least two of $\mathcal{M}$, $\mathcal{P}$, and ω_m to not be conserved. Below we consider how $\mathcal{M}$, $\mathcal{P}$, and ω_m evolve according to the various approximate models. From these results, we determine whether or not each model predicts FD in the spectral mean sense. It is more difficult to obtain analytic results about FD in the spectral peak sense. However, Segur *et al.* [22] noted that in their experiments, the FD in the spectral peak sense was always accompanied by a decrease in $\mathcal{P}$. Thus, our conclusions for FD in the spectral peak sense are based on the evolution of $\mathcal{P}$. These conclusions are consistent with our numerical results that are discussed in Section 4. We also note that in experiments, there is damping, which causes a nearly exponential decay of both $\mathcal{M}$ and $\mathcal{P}$. Thus, we seek a model that predicts both this decay as well as the FD exhibited by an evolving $\mathcal{P}$. The vDysthe equation, (8), the IS equation, (14), and the dGT equation, (15), have all of these ingredients.

The vDysthe equation does not preserve $\mathcal{M}$, $\mathcal{P}$, or ω_m in χ (dimensionless distance down the tank). The χ dependencies of these quantities are given by

$$\frac{d\mathcal{M}}{d\chi} = -2\delta\mathcal{M} - 10\epsilon\delta\mathcal{P}, \tag{17a}$$

$$\frac{d\mathcal{P}}{d\chi} = -2\delta\mathcal{P} - 10\epsilon\delta\mathcal{Q} - 16\epsilon\mathcal{R}, \tag{17b}$$

$$\frac{d\omega_m}{d\chi} = \frac{d}{d\chi}\Big(\frac{\mathcal{P}}{\mathcal{M}}\Big) = -\frac{10\epsilon\delta}{\mathcal{M}^2}\Big(\mathcal{M}\mathcal{Q} - \mathcal{P}^2\Big) - 16\epsilon\frac{\mathcal{R}}{\mathcal{M}}, \tag{17c}$$

where

$$\mathcal{Q} = \frac{1}{L}\int_0^L |B_\xi|^2 d\xi, \tag{18a}$$

$$\mathcal{R} = \mathrm{Im}\Big(\frac{1}{L}\int_0^L |B|^2 B_{\xi\xi} B^* d\xi\Big). \tag{18b}$$

Equation (17a) establishes that to leading order, $\mathcal{M}$ decays exponentially in χ. This allows δ to be determined empirically (see Section 3). Equation (17a) also establishes that $\mathcal{M}$ decreases more rapidly when $\mathcal{P} > 0$ and more slowly when $\mathcal{P} < 0$. This suggests a preference for waves with negative wavenumbers (i.e. $\mathcal{P} < 0$). The first term on the right-hand side of equation (17b) establishes that to leading order, $\mathcal{P}$ decays exponentially in χ. The second term provides a preference for downshifting (over upshifting) in the spectral peak sense, because $\mathcal{Q}$ is positive for all B that are not constant in ξ. This term competes with the term including $\mathcal{R}$, which could either enhance downshifting or cause upshifting, because its sign is indefinite. In (17c), the first term on the right-hand side provides a preference for downshifting (over upshifting) in the spectral mean sense, because the Cauchy-Schwarz inequality establishes that $(\mathcal{M}\mathcal{Q} - \mathcal{P}) \geq 0$. Again, the $\mathcal{R}$ term could either enhance the downshifting or cause upshifting. We note that Ma *et al.* [19] observed upshifting in the spectral peak sense in some of their experiments, so a good model for downshifting should allow for the possibility of both upshifting and downshifting in both the spectral peak and the spectral mean.

Setting $\delta = \epsilon = 0$ in equation (17) shows that the NLS equation preserves $\mathcal{M}$, $\mathcal{P}$, and ω_m. Therefore NLS cannot model frequency downshift in the spectral mean sense. Setting $\epsilon = 0$ in equation (17) establishes that although the dNLS equation does not preserve $\mathcal{M}$ nor $\mathcal{P}$, it preserves ω_m and therefore

cannot model FD in the spectral mean sense either. Setting $\delta = 0$ in (17), but allowing $\epsilon > 0$, recovers the results from the (inviscid) Dysthe equation. Equation (17c) shows that the (inviscid) Dysthe model predicts either upshifting or downshifting in the spectral mean sense. There is no preference for downshifting, which is usually (but not always) observed. We note, however, that the (inviscid) Dysthe model predicts $\mathcal{M}$ to be a constant, which does not agree with experimental observations. It also does not capture the exponential decay of $\mathcal{P}$ observed in small-amplitude experiments.

The IS equation does not preserve $\mathcal{M}$, $\mathcal{P}$, or ω_m. Their χ dependencies are given by

$$\frac{d\mathcal{M}}{d\chi} = -2\delta\mathcal{M} - \frac{2\epsilon\beta_1}{L}\int_0^L |B|^2\Big(\mathcal{H}\big(|B|^2\big)\Big)_\xi d\xi, \tag{19a}$$

$$\frac{d\mathcal{P}}{d\chi} = -2\delta\mathcal{P} - -\frac{i\epsilon\beta_1}{L}\int_0^L \Big(BB_\xi^* - B_\xi B^*\Big)\Big(\mathcal{H}\big(|B|^2\big)\Big)_\xi d\xi, \tag{19b}$$

$$\frac{d\omega_m}{d\chi} = -\frac{2\epsilon\beta_1}{\mathcal{M}^2}\left(\frac{i\mathcal{M}}{2L}\int_0^L \big(BB_\xi^* - B_\xi B^*\big)\Big(\mathcal{H}\big(|B|^2\big)\Big)_\xi\, d\xi - \frac{\mathcal{P}}{L}\int_0^L |B|^2\Big(\mathcal{H}\big(|B|^2\big)\Big)_\xi\, d\xi\right). \tag{19c}$$

Since β_1 is an arbitrary constant, the IS model allows for both FD and FU.

The Gordon equation preserves $\mathcal{M}$, but neither $\mathcal{P}$, nor ω_m. The χ dependencies of these quantities are given by

$$\frac{d\mathcal{P}}{d\chi} = -\epsilon\beta_2\mathcal{S}, \tag{20a}$$

$$\frac{d\omega_m}{d\chi} = -\epsilon\beta_2\frac{\mathcal{S}}{\mathcal{M}}, \tag{20b}$$

where

$$\mathcal{S} = \frac{1}{L}\int_0^L \Big(\big(|B|^2\big)_\xi\Big)^2 d\xi. \tag{21}$$

Equation (20b) establishes that the Gordon equation, with $\beta_2 > 0$, predicts FD in the spectral mean sense for all B except those that have constant modulus in ξ.

The dGT equation does not preserve $\mathcal{M}$, $\mathcal{P}$, or ω_m. Their χ dependencies are given by

$$\frac{d\mathcal{M}}{d\chi} = -2\delta\mathcal{M} - 10\epsilon\delta\mathcal{P} - 20\epsilon^2\delta\mathcal{Q}, \tag{22a}$$

$$\frac{d\mathcal{P}}{d\chi} = -2\delta\mathcal{P} - 10\epsilon\delta\mathcal{Q} - 20\epsilon^2\delta\mathcal{T}, \tag{22b}$$

$$\frac{d\omega_m}{d\chi} = \frac{-10\epsilon\delta\big(\mathcal{M}\mathcal{Q} - \mathcal{P}^2\big) - 20\epsilon^2\delta\big(\mathcal{M}\mathcal{T} - \mathcal{Q}\mathcal{P}\big)}{\mathcal{M}^2}, \tag{22c}$$

where

$$\mathcal{T} = \mathrm{Im}\left(\frac{1}{L}\int_0^L B_{\xi\xi}B_\xi^* d\xi\right). \tag{23}$$

Since $\mathcal{M} \geq 0$ and $\mathcal{Q} \geq 0$, equation (22a) establishes that $\mathcal{M}$ decreases more rapidly when $\mathcal{P} > 0$. This suggests a preference for waves with negative wavenumbers. The Cauchy-Schwarz inequality establishes that $(\mathcal{M}\mathcal{Q} - \mathcal{P}^2) \geq 0$. The Cauchy-Schwarz inequality also establishes that if $\mathcal{P} > 0$, then $(\mathcal{M}\mathcal{T} - \mathcal{Q}\mathcal{P}) \geq 0$ or if $\mathcal{P} < 0$, then $(\mathcal{M}\mathcal{T} - \mathcal{Q}\mathcal{P}) \leq 0$. Therefore, equation (22c) establishes that under the dGT equation, the spectral mean will not increase as long as the $\mathcal{O}(\epsilon^2)$ term is smaller than the $\mathcal{O}(\epsilon)$ term, as it should be.

Another important property of the dGT equation is that all solutions to the linearized dGT equation decay to zero in χ if $\delta > 0$. The linearized vDysthe equation does not have this property. Solutions of the linearized vDysthe equation with wavenumber less than $-\frac{1}{5\epsilon}$ grow exponentially in χ when $\delta > 0$. Wavenumbers in this range are outside of the narrow-bandwidth region where the equation is meant to be valid; nevertheless, it is a limitation of the model.

parameter	Expt A	Expt B	Expt C	Expt D
$\bar{\omega}_{0f}/(2\pi)$ (Hz)	3.33	3.33	3.33	3.33
$\bar{\omega}_{1f}/(2\pi)$ (Hz)	0.17	0.17	0.11	0.11
$\bar{a}_f$ (cm)	0.25	0.25	0.50	0.50
r	0.14	0.33	0.50	0.50

Table 1: Wave maker parameters: carrier wave frequency, $\bar{\omega}_{0f}$; modulation frequency, $\bar{\omega}_{1f}$; forcing amplitude of carrier wave, $\bar{a}_f$; ratio of forcing amplitudes of the modulation to that of the carrier wave, r. In Expt. D, only the upper sideband was forced.

3 Experimental apparatus and results

To test the accuracy of the models, we compare predictions of Fourier amplitudes $\mathcal{M}$, $\mathcal{P}$, ω_p, and ω_m, from the models, with data already in the literature and with two new experiments. Experiments A and B were presented in Segur *et al.* [22] and reconsidered in Carter & Govan [4]. Experiments C and D are new. All four experiments were conducted in the William G. Pritchard Fluid Mechanics Laboratory in the Mathematics Department at Penn State. The procedures for experiments A and B are described in Segur *et al.* [22]. The procedures for experiments C and D are very similar, although the equipment involved was different. The wave channel used for A and B was 43 ft long. The wave channel used for C and D was 50 ft long. Both channels had glass bottoms and sidewalls and were 10 in wide. The tank walls were cleaned with alcohol; then water was added. The air-water interface was cleaned by skimming (A and B) or blowing (C and D) the interfacial layer to one end of the tank where it was vacuumed – the resulting still water depth the for all experiments was 20 cm. Waves were generated in all four experiments with anodized, wedge-shaped plungers that spanned the width of the tank and were oscillated vertically using feed-back, programmable control. The cross-section of the wedge was exponential for A and B (with a fall-off that corresponds to the velocity field for a 3.33 Hz wave) and was triangular for C and D (with a slope corresponding to a linear approximation to the exponential of the paddle for A and B). For Experiments A and B, which used PMAC - Delta Tau Data Systems for motion control, the wedge was oscillated with a time series given by $\bar{\eta}_p(t) = \bar{a}_f \sin(\bar{\omega}_{0f} t)\Big(1 + r\sin(\bar{\omega}_{1f}\bar{t})\Big)$, where $\bar{a}_f$ is the forcing amplitude of the carrier wave, $\bar{\omega}_{0f}$ is the carrier wave frequency, r is the ratio of perturbation amplitude to $\bar{a}_f$, and $\bar{\omega}_{1f}$ is the perturbation frequency. Experiments C and D used ARCS software for motion control. For C, the wedge was oscillated with a time series given by $\bar{\eta}_p(t) = \bar{a}_f \sin(\bar{\omega}_{0f}\bar{t})\Big(1 - r\cos(\bar{\omega}_{1f}\bar{t})\Big)$, and for Experiment D, $\bar{\eta}_p(t) = \bar{a}_f \sin(\bar{\omega}_0\bar{t}) + \bar{a}_f r \sin\Big((\bar{\omega}_{0f} + \bar{\omega}_{1f})\bar{t}\Big)$. The forcing for Experiment D is different so as to purposefully force the upper sideband but not the lower sideband. The forcing amplitudes and frequencies are given in Table 1.

Capacitance-type wave gauges whose signals were imported into LabVIEW were used to measure time series of surface displacement at a point. For Experiments A and B, the gauge was a non-intrusive capacitance-type gauge that spanned 12.7 cm of the width of the tank and 6 mm in the direction of wave propagation. For Experiments C and D, the gauge was an intrusive glass tube, 1.6 mm in outside diameter, which contained a conductor and was sealed at the underwater end. Each of the four experiments consisted of a set of 10-13 experiments with the gauges located $x_m = 128 + 50(m-1)$ for $m = 1, 2, \ldots, M$ centimeters from the wave maker. The values of M for the four experiments are included in Table 2, which contains all of the experimentally measured parameters. The Fourier transforms of the time series were obtained to determine the complex amplitudes of the carrier wave and its sidebands. Their magnitudes were then compared with predictions from numerical computations of the models - the comparisons are shown in Figures 2, 3, 6, and 7 and are discussed in Section 4. Their magnitudes are compared with predictions from numerical computations of the models. We note that both the amplitude and phase of the measurements are required to initialize the numerical computations done for these comparisons. The integrals for $\mathcal{M}$ and $\mathcal{P}$ are obtained using Parseval's theorem, the measured Fourier coefficients at each measurement location, and the notion that the derivatives in $\mathcal{P}$ correspond to multiplication by the corresponding difference frequencies.

parameter	Expt A	Expt B	Expt C	Expt D
M	12	11	13	13
$\bar{k}_0$ (cm^{-1})	0.4478	0.4470	0.4472	0.4472
ϵ	$9.677 * 10^{-2}$	$9.388 * 10^{-2}$	$6.366 * 10^{-2}$	$6.878 * 10^{-2}$
δ	0.2640	0.3223	0.5021	0.8129
N	41	39	50	45
$\bar{t}_f$ (sec)	24.28	23.40	30.00	27.00
BFI	3.919	3.661	4.244	4.127

Table 2: Experimentally measured parameters for each of the four experiments.

Figure 1 contains plots of the surface displacement (in cm) at fixed distances (x+128 cm) from the wave maker as functions of time (in sec) and the corresponding Fourier magnitudes (in cm) versus frequency (in Hertz) for Experiment B. For conciseness, only the results from every other gauge are included. Plots from the other experiments are similar. The plots for Expt. B show that FD in the spectral peak sense occurs between the gauges at $x = 350$ and $x = 450$ because the spectral peak decreases from 3.33 Hz (the carrier wave) to 3.16 Hz (the first lower sideband) between these gauges.

Figures 2-8 show results from experiments (and numerical simulations) of the models. In the rest of this section we discuss the experimental results. The numerical results from the models are compared with the experimental results in Section 4.

Figures 2 and 3 contain plots of the (dimensionless) amplitudes of the carrier wave and the six sidebands with largest amplitudes versus (dimensionless) χ for Experiments C and D respectively. The corresponding plots for Experiments A and B are found in Carter & Govan [4], though they are presented in dimensional form there. In all four experiments, the amplitude of the carrier wave decreases dramatically due to the growth of sidebands and dissipation. By design, in Expt. D, the first upper sideband, $|a_1|$, started with almost twice as much energy as the first lower sideband, $|a_{-1}|$. In Experiments C and D the magnitude of the first upper sideband decreases significantly while the magnitude of the first lower sideband increases slightly. Note that the third lower sideband in Experiment D has a magnitude smaller than experimental error (the wave gauges measure amplitudes down to 0.005 cm). The curves correspond to predictions obtained from the models and are discussed in the next section.

The Benjamin-Feir index (BFI), defined by

$$\text{BFI} = \frac{2\epsilon}{\Delta\bar{\omega}/\bar{\omega}_0}, \tag{24}$$

is relative measure of nonlinearity to spectral bandwidth. If BFI > 1, then the wave train is unstable with respect to the Benjamin-Feir instability. See Janssen [12] and Serio *et al.* [23] for more details on the Benjamin-Feir index. The values of the BFI for the four experiments studied herein are included in Table 2. All four BFI values are greater than 1, so the Benjamin-Feir instability is expected to play a role in all four experiments.

Figure 4 shows how (dimensionless) $\mathcal{M}$ evolves as χ increases for each experiment. The plots show that $\mathcal{M}$ decays nearly exponentially as the waves travel down the tank, i.e. nearly $\mathcal{M}(\chi) = \mathcal{M}(0)\exp(-2\delta\chi)$, for all four experiments. Table 2 contains the least-squares best-fit values of δ. We emphasize that this empirical definition of δ combines all dissipative effects, regardless of their source, into a single term. The mathematical models handle dissipation in a variety of ways. In their derivation, Dias *et al.* [5] determine that $\delta = \frac{4\bar{k}_0^2\bar{\nu}}{\epsilon^2\bar{\omega}_0}$ where $\bar{\nu} = 1.003 * 10^{-1}$ cm^2/sec represents the kinematic velocity of the fluid. This result is consistent with the classical Lamb [17] result for a clean surface. vanDorn [27], shows that the dissipation due to boundary layers along the sidewalls is given by $\delta = \frac{1}{\epsilon^2\bar{\omega}_0}\sqrt{\frac{2\bar{\nu}}{\bar{\omega}_0}}$. The inextensible surface model of Lamb [17] gives $\delta = \frac{\bar{k}_0}{\epsilon^2}\sqrt{\frac{\bar{\nu}}{2\bar{\omega}_0}}$. Table 3 includes a comparison of these theoretical values with the experimentally measured values. The theoretical values require the sum of the sidewall rate plus a rate due to the surface. These sums, using the clean surface value, are also shown in Table 3. These predicted values are in reasonable agreement with measurements from Experiments A and C. See Henderson *et al.* [10] for a more detailed comparison of these and other models of dissipation in water waves.

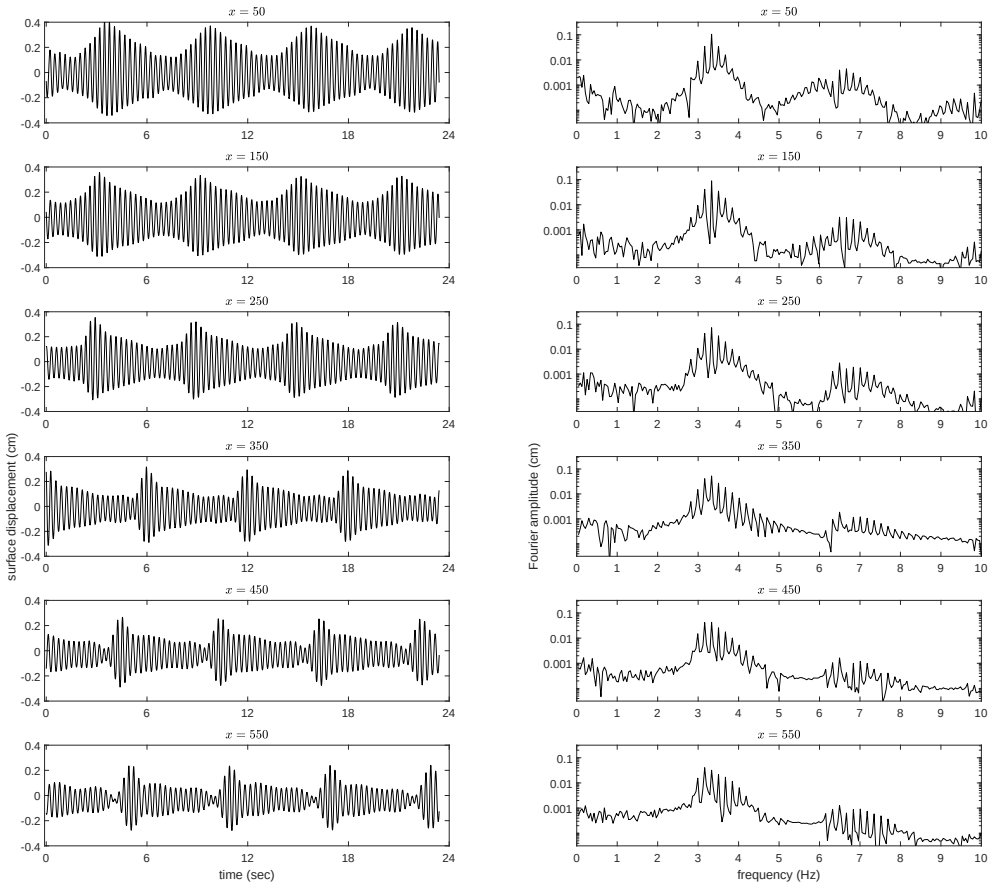

Figure 1: Plots from every other gauge for Expt. B. The first column contains plots of surface displacement (in cm) versus time (in sec). The second column contains plots of the magnitudes of the corresponding Fourier coefficients (in cm) versus frequency (in Hz).

δ	Expt A	Expt B	Expt C	Expt D
Experimental	0.2640	0.3223	0.5021	0.8129
Clean Surface	0.0410	0.0434	0.0945	0.0810
Inextensible Surface	0.7400	0.7849	1.7074	1.4626
Sidewall	0.1854	0.1971	0.4285	0.3671
Clean Surface & Sidewall	0.2264	0.2405	0.5230	0.4481

Table 3: Experimentally and theoretically determined values for δ, the dimensionless decay rate.

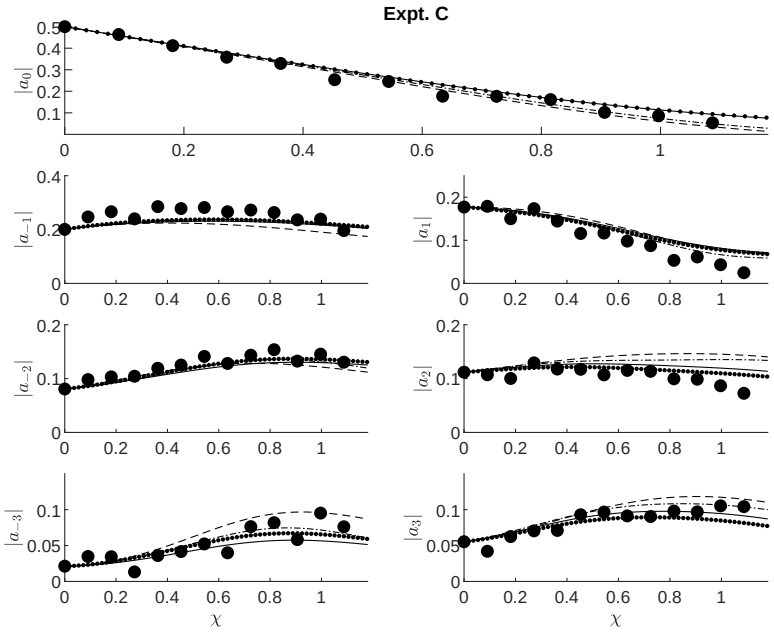

Figure 2: Plots of the nondimensional amplitudes of the carrier wave and the three most energetic sideband pairs versus nondimensional distance down the tank for Expt. C. The large dots correspond to experimental measurements, the dashed curves correspond to dNLS, the solid curves correspond to vDysthe, the dash-dot curves correspond to optimized IS, and the dotted curves correspond to dGT.

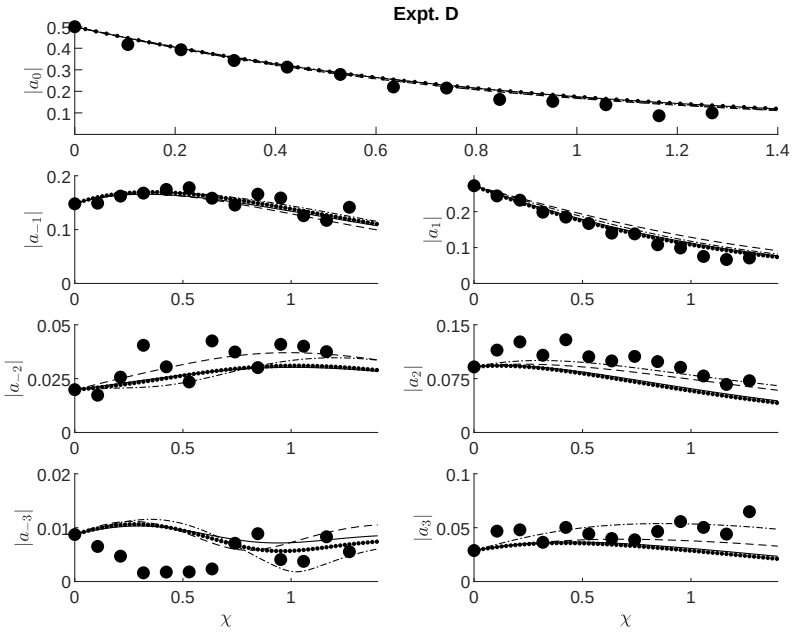

Figure 3: Plots of the nondimensional amplitudes of the carrier wave and the three most energetic sideband pairs versus nondimensional distance down the tank for Expt. D. The large dots correspond to experimental measurements, the dashed curves correspond to dNLS, the solid curves correspond to vDysthe, the dash-dot curves correspond to optimized IS, and the dotted curves correspond to dGT.

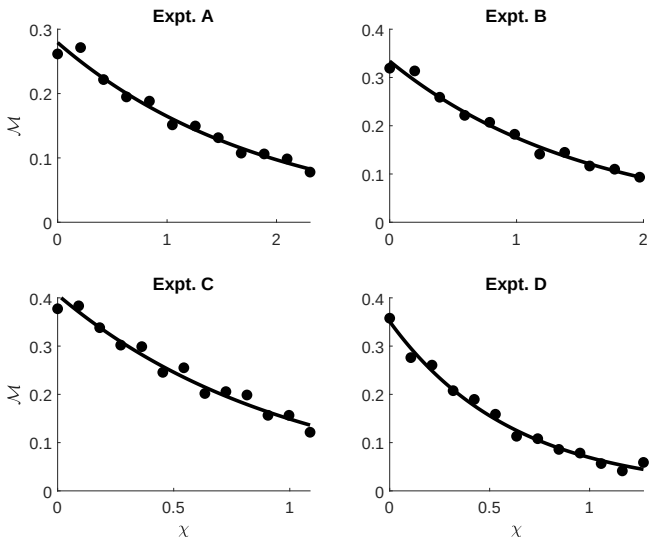

Figure 4: Plots of (dimensionless) $\mathcal{M}$ versus (dimensionless) χ for the four experiments. The dots correspond to experimental measurements and the curves are the best-fit exponentials.

Figure 5 shows how (dimensionless) $\mathcal{P}$ evolves as χ increases for each experiment. In Expt. A, $\mathcal{P}$ remained more or less constant. In Expt. B, $\mathcal{P}$ decreased from a positive value to a negative value. In Expt. C, $\mathcal{P}$ for about half of its evolution, changing sign, and then increased. In Expt. D, $\mathcal{P}$ decreased for a while, then leveled off, and rose at the last gauge. Note that Figure 5 contains plots of unscaled $\mathcal{P}$. This is different than the (exponentially scaled) plots of $\mathcal{P}e^{2\delta\chi}$ included in Segur *et al.* [22]. So, if dissipation was the only factor, we would expect to see exponential decay of $\mathcal{P}$, but we would not expect to see $\mathcal{P}$ change sign.

Figure 6 contains plots of ω_p versus χ for each experiment. The curves are from the various models and are discussed in Section 4. These plots show that Expt. A did not exhibit FD in the spectral peak sense because ω_p was constant at all gauges. Experiments B and D exhibited temporary FD in the spectral peak sense because ω_p decreased, but did not permanently remain lower. However, note that it is possible that this FD would have become permanent had the experimental tank been longer. Expt. C exhibited a permanent FD in the spectral peak sense because the magnitude of the first lower sideband overtook that of the carrier wave and remained dominant.

Figure 7 contains plots of ω_m versus χ. The curves are from the models and are discussed in Section 4. A comparison of Figures 6 and 7 shows that there does not appear to be a relationship between the evolution of ω_p and ω_m. Expt. A did not exhibit FD in the spectral mean sense because ω_m remained essentially constant throughout the experiment. Expt. B exhibited FD in the spectral mean sense because ω_m decreased significantly and even changed sign. Although it is difficult to interpret the final experimental data point, Expt. C exhibited FD in the spectral mean sense because ω_m decreased and changed sign. In Expt. D, ω_m started out more or less constant and then increased dramatically in the last three gauges. This means that Expt. D exhibited frequency upshift in the spectral mean sense near the end of the experiment.

4 Comparison of model and experimental results

All model equations were solved numerically using the high-order operator splitting methods introduced by Yoshida [29]. The linear parts of the PDEs were solved exactly in Fourier space using fast Fourier transforms (FFTs) and the nonlinear parts were either solved exactly in physical space (NLS, dNLS) or solved pseudospectrally using fourth-order Runge-Kutta (Dysthe, vDysthe, dGT, Gordon, IS). Periodic boundary conditions on the (dimensionless) interval $\xi \in [0, \epsilon\bar{\omega}_0\bar{t}_f)$, where $\bar{t}_f$ is the length (in seconds) of

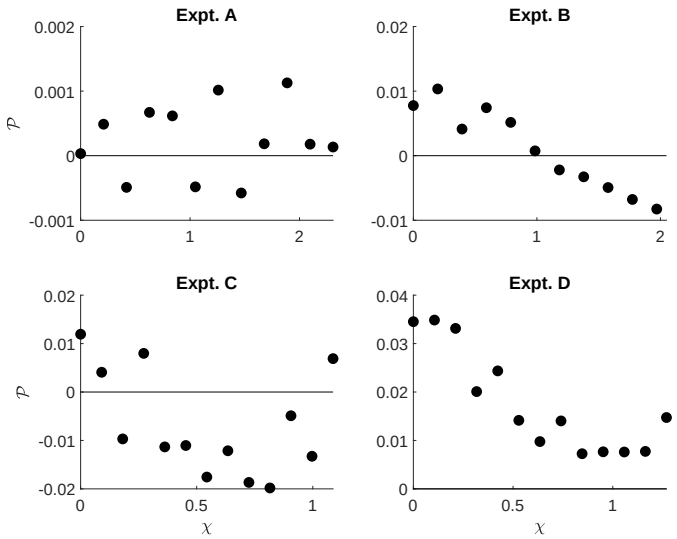

Figure 5: Plots of (dimensionless) $\mathcal{P}$ versus (dimensionless) χ for the four experiments. The horizontal lines correspond to $\mathcal{P} = 0$.

the time series collected at the first gauge, were imposed. The initial conditions were

$$B(\xi, \chi = 0) = \frac{\bar{k}_0}{\epsilon} \sum_{m=-M}^{M} \bar{a}_m \exp\left(im \frac{2\pi}{\epsilon \bar{\omega}_0 \bar{t}_f} \xi\right), \tag{25}$$

where the $\bar{a}_m$ are the coefficients determined by taking an FFT of the time series recorded by the first gauge. Only the $2N + 1$ modes closest to and including the carrier wave (i.e. the modes corresponding to 1.667 to 5.000 Hz) were used in the initial conditions because the models are based on narrow bandwidth assumptions. See Table 2 for the values of $\bar{t}_f$, N, and the other parameters for each experiment.

We start by considering the Gordon model. First, it preserves $\mathcal{M}$ while all four experiments show that $\mathcal{M}$ decays nearly exponentially. Second, the first column of Figure 8 contains plots of (dimensionless) $\mathcal{P}$ versus χ along with the best-fit quadratic function for each experiment. The second column contains plots of the ratio of the experimentally computed $\mathcal{S}$ (see equations (20b) and (21)) over the estimated values of $\frac{d\mathcal{P}}{d\chi}$ obtained using the quadratic functions. Equation (20a) establishes that if the Gordon explanation for downshifting is adequate for water waves, then this ratio would be constant in χ. Since the plots show that the ratio is not constant for any of the experiments, we conclude that one cannot find a constant β_2 so that equation (20a) is satisfied and therefore the Gordon model for FD in optical fibers is not appropriate for FD in waves on deep water. We note that including a term proportional to $i\delta B$ in the Gordon equation will not help, except perhaps for Expt. A which has small amplitudes and does not exhibit downshifting because the Gordon term is negligible. In Experiments B and C, the measured $\mathcal{P}$-values change sign, which cannot be explained by the model with an overall exponential decay. In Expt. D, the predicted $\mathcal{P}$-value changed sign, while the measured values did not.

In order to quantitatively compare the PDE predictions with the experimental time series, we use the following (dimensionless) error norm

$$\mathcal{E} = \frac{1}{M-1} \sum_{m=2}^{M} \sum_{n=-12}^{12} \left| \frac{\bar{k}_0}{\epsilon} \left|\bar{a}_n^{\text{expt}}(m)\right| - \left|a_n^{\text{PDE}}(m)\right| \right|^2, \tag{26}$$

where $a_n^{\text{expt}}(m)$ and $a_n^{\text{PDE}}(m)$ represent the experimentally measured and numerically predicted (using the model PDE) Fourier coefficients of the n^{th} mode at the m^{th} gauge. Since the time series at the first gauge is used to define the initial conditions for the PDEs, the difference between the experimental and

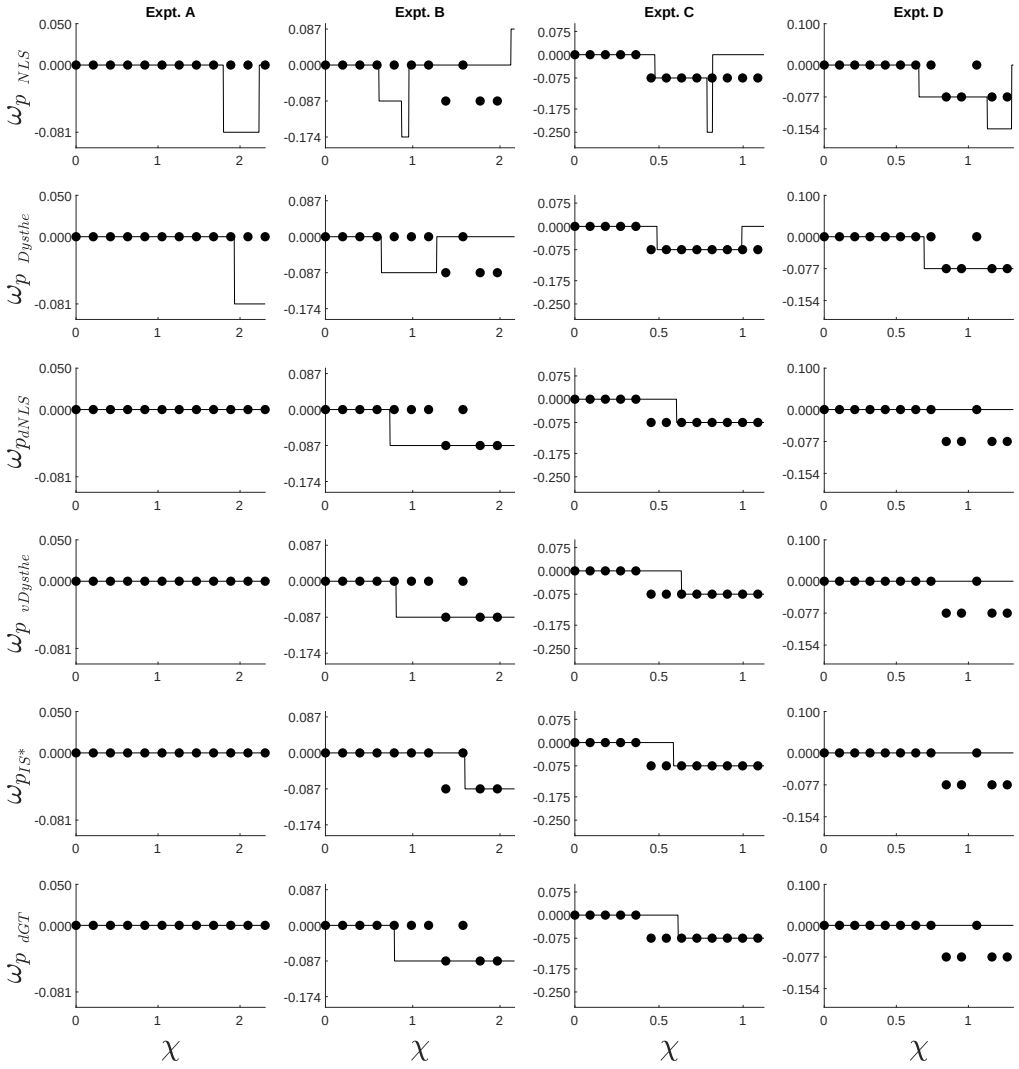

Figure 6: Plots of ω_p versus χ. The columns show results for the four experiments. The rows correspond to the results from NLS, Dysthe, dNLS, vDysthe, IS*, and dGT. The dots correspond to experimental measurements and the lines correspond to the model predictions.

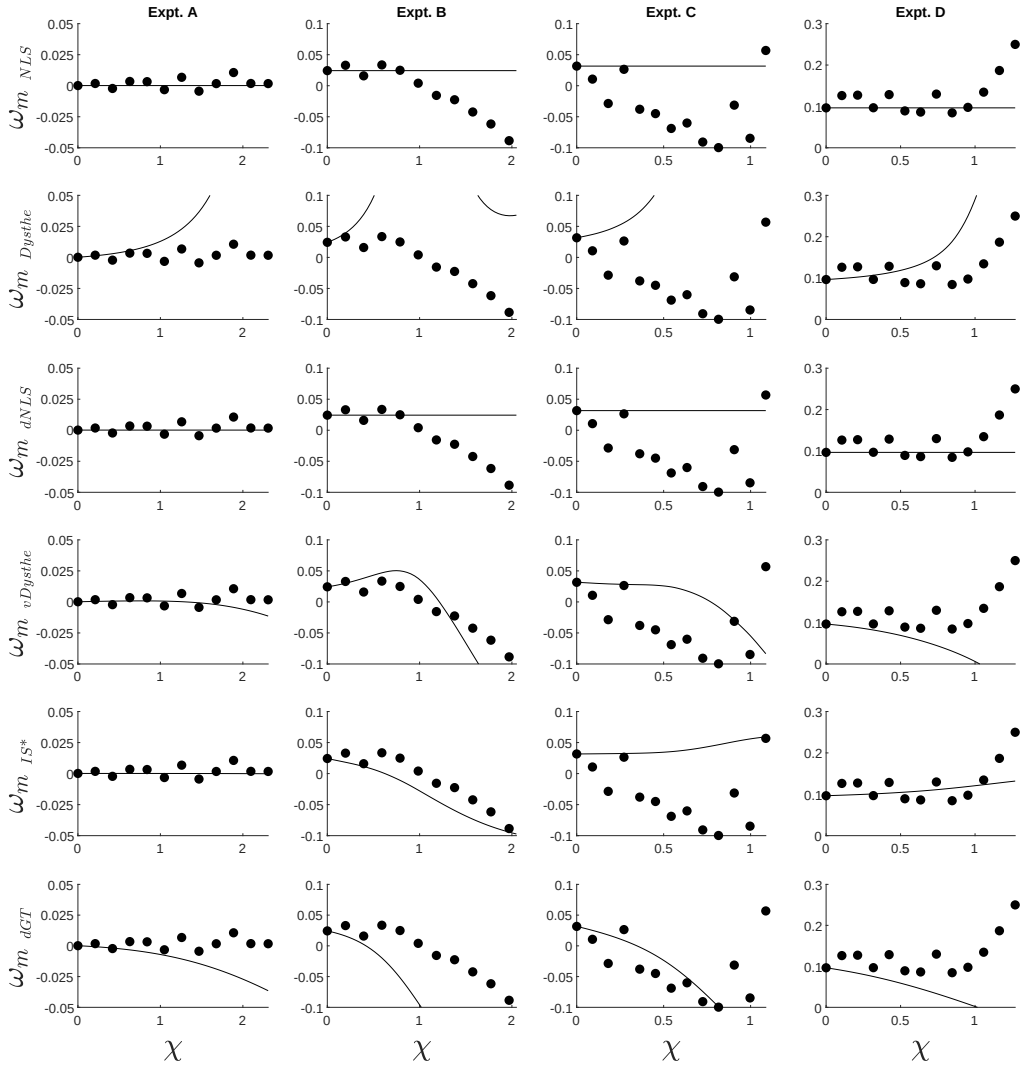

Figure 7: Plots of ω_m versus χ. The columns show results for the four experiments. The rows correspond to the results from NLS, Dysthe, dNLS, vDysthe, IS*, and dGT. The dots correspond to experimental measurements and the curves correspond to the model predictions.

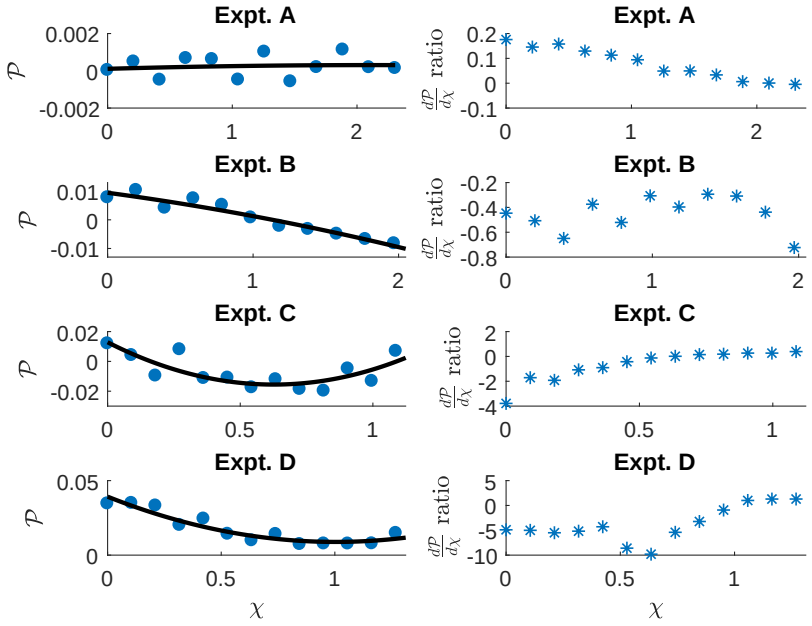

Figure 8: The first column contains plots of $\mathcal{P}$ versus χ for each experiment. The dots correspond to experimental measurements and the curves are the best quadratic fits. The second column contains plots of the ratio of experimentally determined $\mathcal{S}$ and $\frac{d\mathcal{P}}{d\chi}$ estimated using the quadratic fits shown in the first column.

numerical values there is zero and therefore does not need to be included in the sum. In essence, this norm is the L_2 difference of the experimentally measured and numerically predicted magnitudes of the 25 Fourier modes closest to and including the carrier wave averaged across the $M-1$ downstream gauges. These 25 Fourier modes include all of the modes shown in Figures 2 and 3. Table 4 contains the $\mathcal{E}$ values for each of the experiments using the models discussed above.

The Gordon and IS models contain free parameters, β_1 and β_2. Minimizing $\mathcal{E}$ over these parameters leads to what we call the optimized IS, denoted IS*, and optimized Gordon models. The optimal Gordon model is much less accurate than dNLS, vDysthe, IS*, and dGT when measuring error using $\mathcal{E}$. Additionally, the Gordon model leads to wave breaking and poor predictions for the evolution of ω_p and ω_m.

Table 4 shows that IS* provides the minimal $\mathcal{E}$ value for Experiments B, C, and D while vDysthe provides the minimal $\mathcal{E}$ value for Experiment A. The values of β_1 that lead to these results are included in Table 5. As far as we can tell, there is no relation between the four β_1 values and there is no way to determine β_1 from the experimental parameters. In contrast to the Islas-Schober assumption that $\beta_1 > 0$, we note that the optimal value of β_1 for experiments C and D was negative. Figures 2 and 3 shows that IS* accurately predicts the evolution of the carrier wave and the sidebands. Figures 6 and 7 show that IS* has a similar accuracy in predicting the evolution of the spectral peak and mean as do dNLS, vDysthe, and dGT.

Table 4 shows that the NLS and Dysthe models do not accurately model the evolution of the waves in these experiments. Because of this, plots of the NLS and Dysthe predictions were not included in Figures 2 and 3. They greatly over predict the growth of the first sidebands. Additionally, NLS and Dysthe both preserve $\mathcal{M}$, which is not preserved in the experiments.

Figure 6 shows comparisons of the models' predictions of the evolution of the spectral peak with the measurements. In this paragraph, every mention of FD means FD in the spectral peak sense. We note that the nth negative/positive scale markings on the ordinate correspond to the nth lower/upper sideband.

A. Experiment A is the small-amplitude experiment in which FD was not observed. NLS

model	Expt. A	Expt. B	Expt. C	Expt. D
NLS	$4.05 * 10^{-2}$	$8.83 * 10^{-2}$	$6.05 * 10^{-2}$	$8.59 * 10^{-3}$
dNLS	$1.19 * 10^{-3}$	$3.47 * 10^{-2}$	$1.02 * 10^{-2}$	$5.12 * 10^{-3}$
Dysthe	$3.44 * 10^{-2}$	$8.41 * 10^{-2}$	$4.01 * 10^{-2}$	$7.79 * 10^{-2}$
vDysthe	$6.43 * 10^{-4}$	$2.33 * 10^{-2}$	$8.73 * 10^{-3}$	$5.39 * 10^{-3}$
dGT	$7.29 * 10^{-4}$	$2.19 * 10^{-2}$	$7.78 * 10^{-3}$	$5.54 * 10^{-3}$
IS*	$6.75 * 10^{-4}$	$6.14 * 10^{-3}$	$7.72 * 10^{-3}$	$4.45 * 10^{-3}$

Table 4: Comparisons between experimental measurements and numerical predictions using the error norm defined in equation (26). The errors listed for the IS* model is the minimal error found by minimizing (26) over β_1. The optimal values of β_1 are included in Table 5.

model	Expt. A	Expt. B	Expt. C	Expt. D
β_1 (IS*)	0.7	32.0	-2.4	-20.0

Table 5: The β_1 values that minimize $\mathcal{E}$ for the IS* model.

predicts a temporary FD and Dysthe predicts FD, so these models are not in agreement with experimental observations. All of the models that include dissipation agree with the experimental observations: the dNLS, vDysthe, IS, and dGT equations all predict that the spectral peak is constant.

B. The spectral peak in Experiment B downshifts. One data point shows a recurrence and then a return to FD. NLS predicts FD to the first lower sideband, then the second lower sideband, followed by frequency upshift to the first upper sideband shortly after the last experimental gauge. Thus, NLS is not in agreement with observations. Dysthe predicts a temporary FD before it is observed and does not capture the, observed final FD. The dNLS, vDysthe, IS, and dGT equations all predict permanent FD and are thus in qualitative agreement with the observations. However, the dNLS, vDysthe, and dGT equations do not capture the location at which FD is observed to occur. They predict FD to occur too soon. IS* does the best job of capturing the location of the observed FD.

C. The spectral peak in Experiment C downshifts permanently (within the length of the tank), and FD occurs sooner than it does in Experiment B. The NLS and Dysthe equations predict the location of the FD best; however, they predict the FD to be temporary. The other models do not capture the location at which FD is observed, but do predict it to be permanent.

D. In Experiment D the upper sideband was purposefully seeded; nevertheless, the spectral peak in that experiment downshifted. As in Experiment B, one data point shows a recurrence and then a return to FD. NLS predicts a temporary FD to the first and then to the second lower sideband, in disagreement with the observations. Dysthe accurately predicts both the location and the permanence of the observed FD. The other models disagree with observations; they predict a constant spectral peak.

Figure 7 shows comparisons of the models' predictions of the evolution of the spectral mean with the measurements. In this paragraph, every mention of FD means FD in the spectral mean sense. We note that both the NLS and dNLS equations preserve ω_m and therefore, predict that ω_m remains constant throughout each experiment. The Dysthe equation predicts substantial upshifting for all four experiments.

A. Experiment A is the small-amplitude experiment in which the spectral mean remained about constant. Therefore, the Dysthe equation necessarily does not agree with observations. The dGT equation predicts FD and so, also does not agree. The vDysthe equation predicts a slight FD near the end of the observed evolution. The NLS and dNLS necessarily agree with the observations, and here, the IS* equation also agrees.

Model	Fourier Amplitudes (Figures 2 and 3)	$\mathcal{M}$	ω_p (Figure 6)	ω_m (Figure 7)
NLS	0	0	0	A
Dysthe	0	0	C, D	D
dNLS	A, B, C, D	A, B, C, D	A, B, C	A
vDysthe	A, B, C, D	A, B, C, D	A, B, C	A, B, C
IS*	A, B, C, D	A, B, C, D	A, B, C	A, B, D
dGT	A, B, C, D	A, B, C, D	A, B, C	B, C

Table 6: Qualitative summary of results. 0 means qualitative disagreement of predictions from the model (row) with the measure listed (column) for all 4 experiments. The letters correspond to experiments in which there was at least some overall qualitative agreement.

B. The spectral mean in Experiment B downshifts and actually changes sign. Thus, the NLS, dNLS and Dysthe models necessarily disagree with the observations. The vDysthe model predicts a slight upshifting before FD finally takes over. Both the IS* and dGT models predict FD – the IS* predictions are in fairly good agreement with observations, while the dGT predictions substantially over predict the measured FD.

C. The spectral mean in Experiment C downshifts initially and then upshifts to just above its initial value. Thus, the NLS, dNLS and Dysthe models necessarily disagree with the observations. For this experiment, the IS* equation does not capture the initial, significant FD. Both the vDysthe and dGT equations do capture the initial FD, with the dGT predictions agreeing best, but neither of these models predict the observed ending evolution.

D. In Experiment D the upper sideband was purposefully seeded, and the spectral mean shows the consequences. Unlike the spectral peak, the spectral mean exhibits a permanent upshifting. Thus, the NLS, dNLS models necessarily disagree with the observations. The Dysthe equation predicts upshifting and is in qualitative agreement. Both the vDysthe and dGT models predict FD, so they disagree with observations. The IS* equation predicts a slight upshifting, but under predicts the amount of upshifting observed.

5 Summary

In summary, we have compared experimental measurements with a variety of models for the evolution of wave trains on deep water in order to gain a deeper understanding of frequency downshifting. Table 6 contains a summary of our qualitative results. We showed that the NLS equation does not accurately predict the evolution of the major Fourier amplitudes. Nor can it predict FD in the spectral peak sense. The Dysthe equation does not accurately predict the evolution of the major Fourier amplitudes or the spectral mean. The Gordon equation, which comes from optics, does not accurately model the experimental data, even when optimized over its free parameter and cannot accurately model FD in water waves because of how it models the evolution of $\mathcal{P}$. We showed that the dNLS equation accurately models the Fourier amplitudes in all four experiments, but cannot model FD in the spectral mean sense. The viscous Dysthe equation accurately modeled the evolution of the Fourier amplitudes, reasonably predicted the evolution of the spectral peak in all four experiments, and reasonably predicted the spectral mean in three of the four experiments. The dissipative Gramstad-Trulsen equation, introduced in equation (15), accurately models the evolution of the Fourier amplitudes and reasonably predicted the evolution of the spectral peak in all four experiments, and reasonably predicted the spectral mean in three of the four experiments. Finally, the Islas-Schober equation most accurately models the experimental data in three of the four data sets when optimized over its free parameter. Unfortunately, there is not an empirical way to determine this parameter. All of the models are derived with either some ad-hoc term or a free-parameter, and none of the modes captures all of the features of all of the experiments, so a derivation from first principles remains an open problem.

6 Acknowledgements

We thank Bernard Deconinck, Paul Milewski, and Harvey Segur for helpful discussions. This material is based upon work supported by the National Science Foundation under grant DMS-1716120 and DMS-1716159.

References

[1] M. J. Ablowitz and H. Segur. *Solitons and the Inverse Scattering Transform*. SIAM, Philadelphia, 1981.

[2] M. Brunetti and J. Kasparian. Modulational instability in wind-forced waves. *Physics Letters A*, 378:3626–3630, 2014.

[3] M. Brunetti, N. Marchiando, N. Berti, and J. Kasparian. Nonlinear fast growth of water waves under wind forcing. *Physics Letters A*, 378:1025–1030, 2014.

[4] J. D. Carter and A. Govan. Frequency downshift in a viscous fluid. *European Journal of Mechanics - B/Fluids*, 59:177–185, 2016.

[5] F. Dias, A. I. Dyachenko, and V. E. Zakharov. Theory of weakly damped free-surface flows: A new formulation based on potential flow solutions. *Physics Letters A*, 372:1297–1302, 2008.

[6] K. B. Dysthe. Note on a modification to the nonlinear Schrödinger equation for application to deep water waves. *Proceedings of the Royal Society of London A*, 369:105–114, 1979.

[7] J. P. Gordon. Theory of the soliton self-frequency shift. *Optics Letters*, 11(10):662–664, 1986.

[8] O. Gramstad and K. Trulsen. Hamiltonian form of the modified nonlinear Schrödinger equation for gravity waves on arbitrary depth. *Journal of Fluid Mechanics*, 670:404–426, 2011.

[9] T. Hara and C. C. Mei. Frequency downshift in narrow banded surface waves under the influence of wind. *Journal of Fluid Mechanics*, 230:429–477, 1991.

[10] D. Henderson, G. K. Rajan, and H. Segur. Dissipation of narrow-banded surface water waves. *Fields Institute Communications*, 75:163–183, 2015.

[11] A. Islas and C. M. Schober. Rogue waves and downshifting in the presence of damping. *Natural Hazards and Earth System Sciences*, 11:383–399, 2011.

[12] P. A. E. M. Janssen. Nonlinear four-wave interactions and freak waves. *Journal of Physical Oceaongraphy*, 33(4):863–884, 2003.

[13] Y. Kato and M. Oikawa. Wave number downshift in modulated wavetrain through a nonlinear damping effect. *Journal of the Physical Society of Japan*, 64:4660–4669, 1995.

[14] O. Kimmoun, H. C. Hsu, B. Kibler, and A. Chabchoub. Nonconservative higher-order hydrodynamic modulation instability. *Physical Review E*, 96:022219, 2017.

[15] B. M. Lake and H. C. Yuen. A note on some nonlinear water-wave experiments and the comparison of data with theory. *Journal of Fluid Mechanics*, 83:75–81, 1977.

[16] B. M. Lake, H. C. Yuen, H. Rungaldier, and W. E. Ferguson. Nonlinear deep water waves: theory and experiment. Part 2. Evolution of a continuous wave train. *Journal of Fluid Mechanics*, 83:49–74, 1977.

[17] H. Lamb. *Hydrodynamics*. Dover, New York, 1993.

[18] E. Lo and C. C. Mei. A numerical study of water-wave modulation based on a higher-order nonlinear Schrödinger equation. *Journal of Fluid Mechanics*, 150:395–416, 1985.

[19] Y. Ma, G. Dong, M. Perlin, X. Ma, and G. Wang. Experimental investigation on the evolution of the modulation instability with dissipation. *Journal of Fluid Mechanics*, 711:101–121, 2012.

[20] W. K. Melville. The instability and breaking of deep-water waves. *Journal of Fluid Mechanics*, 115:165–185, 1982.

[21] F. M. Mitschke and L. F. Mollenauer. Discovery of the soliton self-frequency shift. *Optics Letters*, 11:659–661, 1986.

[22] H. Segur, D. Henderson, J. D. Carter, J. Hammack, C. Li, D. Pheiff, and K. Socha. Stabilizing the Benjamin-Feir instability. *Journal of Fluid Mechanics*, 539:229–271, 2005.

[23] M. Serio, M. Onorato, A. R. Osborne, and P. A. E. M. Janssen. On the computation of the Benjamin-Feir Index. *Nuovo Cimento-Societa Italiana di Fisica Sezione C*, 28(6):893–903, 2005.

[24] M. Y. Su, M. Bergin, P. Marler, and R. Myrick. Experiments on nonlinear instabilities and evolution of steep gravity-wave trains. *Journal of Fluid Mechanics*, 124:45–72, 1982.

[25] C. Sulem and P. L. Sulem. *The nonlinear Schrödinger equation*. Springer, New York, 1991.

[26] K. Trulsen and K. B. Dysthe. Frequency down-shift through self modulation and breaking. In *NATO ASI Series 178*, pages 561–572, 1990.

[27] W. G. vanDorn. Boundary dissipation of oscillatory waves. *Journal of Fluid Mechanics*, 24:769–779, 1966.

[28] G. Wu, Y. Liu, and D. K. Yue. A note on stabilizing the Benjamin-Feir instability. *Journal of Fluid Mechanics*, 556:45–54, 2006.

[29] H. Yoshida. Construction of higher order sympletic integrators. *Physics Letters A*, 150:262–268, 1990.

[30] V. E. Zakharov. Stability of periodic waves of finite amplitude on the surface of a deep fluid. *Journal of Applied Mechanics and Technical Physics*, 9(2):190–194, 1968.